Stanford Exploration Project, Report 125, January 16, 2007, pages 29–53

Waveform inversion by one-way wavefield extrapolation

Jeff Shragge

ABSTRACT

Forward modeling in frequency-domain waveform inversion is often implemented using finite difference (FD) methods. However, the cost of FD modeling remains too expensive for typical 3D seismic data volumes. One-way wavefield extrapolation is an alternative forward-modeling strategy considerably cheaper to implement. This approach, though, comes with caveats that typically include lower accuracy at steep propagation angles in laterally varying media, a difficulty for incorporating source radiation patterns, and an inability to propagate turning or multiply reflected waves. Each of these factors can play a role in determining the success or failure of a waveform inversion analysis. This study examines the potential for using one-way Riemannian wavefield extrapolation (RWE) operators in the forward modeling component of frequency-domain waveform inversion. RWE modeling is carried out on computational meshes designed to conform to the general direction of turning-wave propagation, which enables the calculation of the direct arrivals, wide-angle reflections and refractions important for a successful waveform inversion. The waveform inversion procedure otherwise closely resembles conventional frequency-domain approaches. Forward modeling test results indicate that RWE waveforms match fairly well with those generated by FD modeling at wider offsets. Preliminary tests of a RWE waveform inversion scheme demonstrate its ability to invert FD-generated synthetic data for moderate (10%) 1D velocity perturbations.

INTRODUCTION

Accurately imaging the Earth's subsurface using seismic wavefield data requires estimating realistic velocity profiles. Most information used to ascertain velocity models, however, derives from two sources: inverting a subset of the seismic wavefield (e.g., first-arrival tomography or waveform inversion), or from a measure of migration image quality (e.g., residual migration or migration velocity analysis). All approaches are nevertheless subject to the non-linearity of the seismic imaging problem and often require multiple iterations of velocity estimation, migration and image quality assessment before converging toward a well-resolved velocity model and seismic image.

One established data-domain approach for velocity estimation is ray-based, first-arrival, travel-time tomography, where earliest arrival times predicted by a linearized theory are matched to those picked from data. Travel-time discrepancies (or residuals) are back-projected along calculated ray-paths for all source and receiver combinations to obtain a velocity model update.

Although iterative ray-based tomography is computationally efficient and can demonstrably recover longer-wavelength velocity profile structure, it has a limited ability to resolve finer-scale model components. Although this shortcoming is partially addressed by more "wave-like" corrections to the asymptotic ray theory, a more accurate (but more expensive) way to improve inverted velocity model resolution is using methods derived from finite-frequency approaches.

A popular alternative to ray-based tomography is waveform inversion based on wave-equation tomography. Assuming a linearized theory, this approach aims to match waveforms modeled by band-limited propagation operators to acquired seismic data. Importantly, higher-resolution velocity models can be recovered where a greater percentage of the seismic wavefield is used in the inversion. (In fact, velocity models developed from ray-based tomography often are the starting models for waveform inversion.) Waveform inversion can be implemented in either the time domain (Tarantola, 1984; Bunks et al., 1985; Mora, 1987; Shipp and Singh, 2002) or in the frequency domain (Pratt and Worthington, 1989; Liao and McMechan, 1996; Sirgue and Pratt, 2004) and for either acoustic and elastic wave equations. Frequency-domain approaches have the benefit that only a limited number of frequencies need be inverted (Pratt and Worthington, 1989), usually starting at lower frequencies then moving up a sparsely sampled spectrum. Moreover, because data are more linear with respect to model parameters at lower frequencies, convergence toward the global minimum is more likely (Sirgue and Pratt, 2004).

Two drawbacks to the general waveform inversion procedure are the memory requirements and computation complexity required to solve the 3D forward modeling problem. Most frequency-domain procedures employ finite-differences (FD) to solve the acoustic or elastic wave-equation, and often implement a LU decomposition of the correspondingly large, but relatively sparse, impedance matrix. The memory requirement for a LU decomposition of a 2D matrix is roughly proportional to nx^4, where nx is the average model space dimension. This can be lowered to roughly nx^3 using graph theoretic techniques able to exploit matrix sparsity (Štekl and Pratt, 1998). The memory requirement for 3D problem, however, theoretically rises to approximately nx^6, which remains too costly for common exploration model sizes. However, novel iterative approaches may be able to reduce the cost of 3D FD modeling (see, e.g., Plessix (2006)).

An alternate way to lower the forward modeling costs is to replace FD modeling with an extrapolation scheme based on propagators derived from one-way wave-equations. Although one-way wavefield extrapolation is not as accurate, the numerical cost of a 3D implementation is roughly $nsnx^3(log_2(nx))^2$ (Biondi, 2006), where ns is the number of shots. Moreover, the memory requirement is now of a similar or lower order of magnitude, and is no longer the impeding constraint. Accordingly, wavefield extrapolation potentially offers significant computational and memory savings and is worth examining in the context of waveform inversion. One-way extrapolation, nevertheless, comes with caveats. For example, long-offset seismic data usually contain turning waves, wide-angle reflections, and forward-scattering from shorter wavelength structure that carry important and complementary information about velocity structure. However, accurately modeling these waves with conventional wavefield extrapolation techniques remains difficult (though not impossible, see Zhang et al. (2006)).

One approach is to use Riemannian wavefield extrapolation (Sava and Fomel, 2005) on a generalized coordinate mesh oriented in the general direction of turning-wave propagation. Because these grids are designed to incorporate the bulk of the turning-wave propagation directly into the coordinate system, it allows the user to implement lower-order extrapolation operators while achieving more accurate global propagation. In addition, one can avoid modeling at depths greater than those of the deepest turning waves, beyond which the transmission wavefield is insensitive to velocity variations (Mulder and Plessix, 2006).

This paper examines the use of one-way Riemannian wavefield extrapolation (RWE) operators in the forward modeling component of frequency-domain waveform inversion. The paper begins with a general review of the Pratt and Worthington (1989) approach. Subsequently, I describe the implementation of RWE forward modeling and present results of tests on the SMAART JV Pluto 1.5 dataset that indicate that RWE waveforms are fairly well matched with those from FD modeling at wider offsets. I then discuss results of a RWE waveform inversion scheme and demonstrate its ability to invert for a moderate (10%) 1D velocity perturbation assuming an *a priori* constant velocity background.

REVIEW OF FREQUENCY-DOMAIN WAVEFORM INVERSION

This section reviews the basic steps of non-linear frequency-domain waveform inversion. The reader wishing to have a more formal overview is referred to Pratt and Worthington (1989), Liao and McMechan (1996), Sirgue and Pratt (2004), and references therein. The technique described herein is modeled after the algorithm of Pratt and Worthington (1989) and uses the notation of Sirgue and Pratt (2004). Additional steps in the inverse approach are drawn from time-domain waveform inversion method of Mora (1987).

Forward modeling

The initial step in frequency-domain waveform inversion is to prescribe the forward model. I assume that wave propagation is adequately governed by the acoustic wave equation; thus, any forward-modeling procedure will generate a monochromatic scalar wavefield, Ψ, that is an (approximate) complex-valued solution to the Helmholtz equation,

$$\mathbf{L}\Psi(\mathbf{s},\mathbf{x};\omega) = \left(\nabla^2 + \frac{\omega^2}{c^2(\mathbf{x})}\right)\Psi(\mathbf{s},\mathbf{x};\omega) = -\delta(\mathbf{s}-\mathbf{x}), \tag{1}$$

where $\mathbf{L}$ is the Helmholtz operator, ∇^2 the Laplacian operator, ω angular frequency, $c(\mathbf{x})$ the assumed velocity profile in spatial domain $\mathbf{x}$, $\mathbf{s}$ the source position, and δ the Dirac delta function operator. Note that the waveform inversion problem is non-linear in model parameters, $m(\mathbf{x}) = c^{-2}(\mathbf{x})$, which I will solve using an iterative inversion approach. Discussion of the specific approach to solving equation 1 being presented is deferred to the following section.

The next step is to compare the modeled wavefield solutions, $\Psi_{calc}(\mathbf{s},\mathbf{r};\omega)$, to the observed data, $\Psi_{obs}(\mathbf{s},\mathbf{r};\omega)$, where $\mathbf{r}$ is the receiver position. This procedure leads to a residual wave-

field, $\Delta\Psi(\mathbf{s},\mathbf{r};\omega)$, defined as the difference between the two wavefields

$$\Delta\Psi(\mathbf{s},\mathbf{r};\omega) = \Psi_{calc}(\mathbf{s},\mathbf{r};\omega) - \Psi_{obs}(\mathbf{s},\mathbf{r};\omega). \tag{2}$$

The residuals are a measure of waveform fit and will be back-projected to generate a velocity model update. Note that no assumption is explicitly made about a linear relation (i.e. the Born approximation is explicitly avoided in the forward modeling problem) (Sirgue and Pratt, 2004); however, if model parameters are too far removed from the true velocity model, then the monochromatic wavefields in equation 2 will cycle-skip giving erroneous residuals. However, because cycle-skipping is more likely at higher frequencies, the approach is generally more stable at lower frequencies.

The Inverse Problem

The approach to solving the waveform inversion problem followed here (Pratt and Worthington, 1989) is based on minimizing the residual misfit at each successive frequency, $E(\omega)$. Assuming an L_2 norm, the misfit is defined

$$E(\omega) = \frac{1}{2}\sum_s\sum_r \Delta\Psi^*(\mathbf{s},\mathbf{r};\omega)\Delta\Psi(\mathbf{s},\mathbf{r};\omega), \tag{3}$$

where $\Delta\Psi^*$ denotes complex conjugate of wavefield $\Delta\Psi$. In this study, I approach the minimization of $E(\omega)$ through computing the negative gradient, or the direction of greatest decrease of the misfit function, with respect to the variation in model parameters. If model parameters are represented by $m(\mathbf{x})$, then the descent direction is defined by

$$g(\mathbf{x}) = -\nabla_m E = -\frac{\partial E}{\partial m(\mathbf{x})}. \tag{4}$$

The gradient vector, $g(\mathbf{x})$, is considered an image of the model space and can be used to update the model parameter estimates according to

$$m_{n+1}(\mathbf{x}) = m_n(\mathbf{x}) + \gamma_n(\mathbf{x})g_n(\mathbf{x}), \tag{5}$$

where $\gamma_n(\mathbf{x})$ is the step length discussed below, and subscript n indicates the current iteration number.

Gradient Vector Definition

Methods for calculating the gradient without explicitly computing the partial derivatives of the data are well established (Lailly, 1983; Tarantola, 1984; Pratt and Worthington, 1989; Pratt et al., 1998). The main result in the time-domain inversion literature is that the gradient vector can be computed by a zero-lag correlation of the wavefield propagated forward from the source point, $P_f(\mathbf{s},\mathbf{x};\omega)$, and the residual wavefield propagated backwards from the farthest receiver

location toward the source point past each successive receiver, $P_b(\mathbf{x},\mathbf{r};\omega)$. The frequency-domain equivalent to this zero-lag correlation is the multiplication of these two wavefields according to

$$g(\mathbf{x};w) = -\omega^2 \sum_s \sum_r Re\left(P_f^*(\mathbf{s},\mathbf{x};\omega) P_b(\mathbf{s},\mathbf{x},\mathbf{r};\omega)\right), \tag{6}$$

where *Re* indicates the real component of the multiplication result. The summation over sources and receivers is done for each non-linear iteration at each frequency. Following Sirgue and Pratt (2004) in assuming a point source of unit amplitude and zero phase, the forward-propagated wavefield P_f is given by

$$P_f(\mathbf{s},\mathbf{x};\omega) = G_0(\mathbf{s},\mathbf{x};\omega), \tag{7}$$

while back-propagated wavefield P_b is defined by

$$P_b(\mathbf{s},\mathbf{x},\mathbf{r};\omega) = G_0^*(\mathbf{x},\mathbf{r};\omega)\Delta\Psi(\mathbf{s},\mathbf{r};\omega), \tag{8}$$

where $G_0(\mathbf{s},\mathbf{x};\omega)$ and $G_0(\mathbf{x},\mathbf{r};\omega)$ represent the monochromatic Green's functions for an excitation at the source and receiver points in the medium, respectively. Hence, the full gradient vector expression is

$$g(\mathbf{x};\omega) = -\omega^2 \sum_s \sum_r Re\left(G_0^*(\mathbf{s},\mathbf{x};\omega) G_0^*(\mathbf{x},\mathbf{r};\omega)\Delta\Psi(\mathbf{s},\mathbf{r};\omega)\right). \tag{9}$$

Note that $G_0^*(\mathbf{x},\mathbf{r};\omega)\Delta\Psi(\mathbf{s},\mathbf{r};\omega)$ represents the back-projection of the data residuals and is similar to a "migration with the residual wavefield data" (Mora, 1987).

Conjugate Gradient Definition

The use of conjugate gradients helps to speed convergence by choosing a direction that is a linear combination of the past and current steepest descent vectors (Luenberger, 1984). Following Mora (1987), I use a conjugate gradient approach given by Polak and Ribiére (1969)

$$c_n = g_n + g_n^* \frac{(g_n - g_{n-1})}{g_{n-1}^* g_{n-1}}, \tag{10}$$

where c_n is the conjugate gradient update. Note that this is equivalent to the formulation in Mora (1987) where data and model space covariances are represented by identity operators. Equation 5 thus modifies to

$$\begin{aligned} m_{n+1}(\mathbf{x}) = &\quad m_n(\mathbf{x}) + \gamma_n(\mathbf{x}) c_n(\mathbf{x}), \quad n \geq 2, \\ = &\quad \gamma_n(\mathbf{x}) g_n(\mathbf{x}), \qquad n = 1. \end{aligned} \tag{11}$$

The computation of conjugate gradient direction in equation 11 comes essentially at no cost because the previous gradient vector, g_{n-1}, easily can be stored in memory.

Step-length Definition

After computing the (conjugate) gradient vector, one must calculate the step length, $\gamma_n(\mathbf{x})$, used to update model parameters (equation 5). This computation is not straightforward because the acoustic wave equation is non-linear in model parameters $m(\mathbf{x}) = c^{-2}(\mathbf{x})$ and the Frechét derivatives are never explicitly calculated. One approach is to use a linear approximation technique based on perturbation methods (Mora, 1987). This involves calculating an approximate Frechét derivative, $\hat{F}$, by performing an additional forward modeling using a set of model parameters perturbed by a scaled version of the computed conjugate gradient (i.e. $m_n(\mathbf{x}) + \eta c_n(\mathbf{x})$) and comparing the result with the initial forward modeled data. This is summarized notationally as

$$\hat{F}_n = \mathbf{L}(m_n + \eta c_n) - \mathbf{L}(m_n) = \Psi_{pert} - \Psi_{orig}, \tag{12}$$

where Ψ_{pert} and Ψ_{orig} are the perturbed and original wavefields, respectively. Perturbation scaling factor η is constrained to be within 1% of the current model parameter values. The step-length is then given by Mora (1987)

$$\gamma_n = \frac{c_n^* g_n}{\frac{1}{\eta^2}\hat{F}_n^* \hat{F}_n + c_n^* c_n}. \tag{13}$$

Again, the step-length in equation 13 is equal to that in Mora (1987) where covariance matrices are represented by identity operators.

General approach to waveform inversion

The above section presented the approach to frequency-domain waveform inversion used in this study. The general computational flow is described the pseudo-code in figure 1. The procedure begins with the forward wavefield modeling (equation 1) for the first non-linear iteration at the first frequency. Wavefield residuals are then computed (equation 2) and back-projected throughout the model volume (the adjoint of equation 1), enabling the computation of the single-source gradient vector (equation 9). This procedure is repeated for all shot points until the total gradient field is computed by stacking single-source gradient profiles. The conjugate gradient direction is then calculated from the current and past gradient vectors (equation 11), and the step length is computed by summing the forward modeling results of the linear perturbation Frechét matrix (equation 12). This process is repeated for the desired number of iterations, or until convergence is reached. The entire process is then repeated at the next highest frequency until inversion of all chosen frequencies is complete.

SOLVING THE FORWARD MODELING PROBLEM

A key development in frequency-domain waveform inversion methodology would be establishing a more rapid, yet accurate, forward modeling approach for generating Helmholtz equation solutions. This is important because, for each non-linear iteration and frequency, forward

```
For all frequencies {
  For all non−linear iterations {
    For all shots {
      Forward model wavefield
      Compute residuals
      Back−propagate residuals
      Compute single−shot gradient
    }
    Sum total gradient vector
    Calculate conjugate gradient
    For all shots {
      Compute single−shot step−length
    }
    Sum total step−length
    Update model
  }
}
```

Figure 1: Flow chart describing the processing flow for waveform inversion. jeff1-flowchart [NR]

modeling is required (at least) three times: i) forward-propagating wavefield P_s to generate data Ψ_{calc}; ii) back-projecting wavefield residuals P_r; and iii) calculating step length γ. In this study, I solve the forward modeling problem using more efficient, though less accurate, one-way extrapolation operators. The central supposition is that the lower accuracy associated with one-way operators will be more than offset by efficiency gains and lower memory requirements of finding waveform inversion solutions. A more fundamental question is whether one-way operators are sufficiently accurate to permit waveform inversion. Demonstrating this assumption's validity is a key result of this paper.

One useful strategy for developing effective one-way operators is to consider propagation in a coordinate system geometry other than Cartesian. For example, one can specify a sideways-tilted, ray-like mesh where the extrapolation axis is predominately oriented in the direction of turning-wave propagation. In this reference frame, the bulk of wavefield continuation occurs at low angles to the extrapolation axis where one-way operators remain accurate. Wavefield propagation on non-Cartesian grids falls under the purview of RWE, which incorporates mesh geometry directly into the Helmholtz equation through additional spatially varying coefficients. The differential geometry used to describe coordinate system transformations in general space is presented in Appendix A, while the operators used in the one-way RWE approach are developed in Appendix B.

Figure 2 illustrates the geometric transformation between Cartesian (two left panels) and RWE domains (two right panels). The upper left panel shows a coordinate system mesh overlying part of the Pluto velocity model. The upper right panel shows this mesh unfolded to form a regular grid, underlying which is the interpolated velocity profile. (The RWE coefficients in Appendix B describe the stretching effects generated by this transformation.) The bottom right panel shows four superimposed wavefield snapshots (at 1.0s, 2.2s, 3.4s and 4.6s) for a

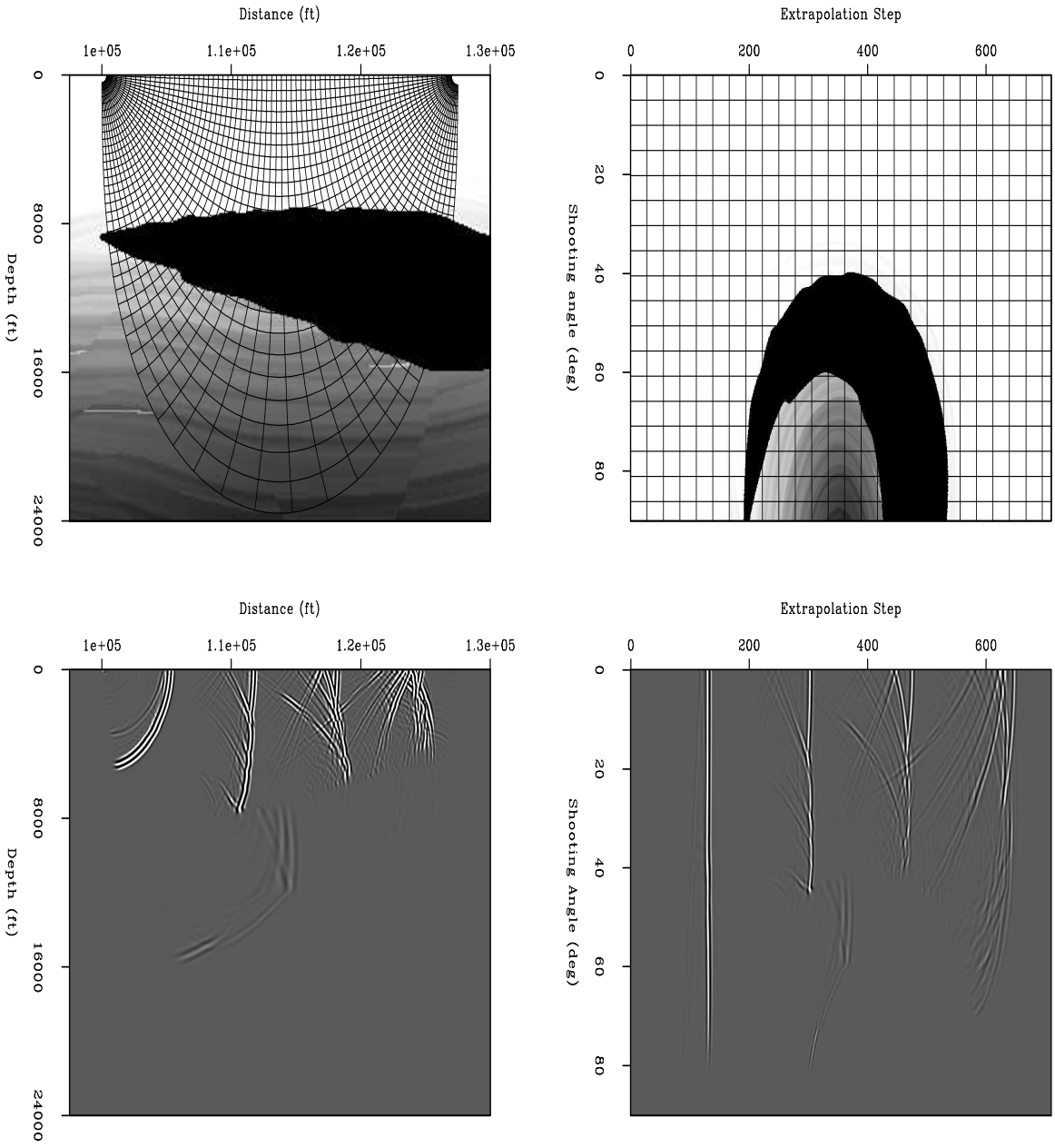

Figure 2: Illustration of the waveform inversion forward modeling approach. The left (right) panels represent the Cartesian (Riemannian) viewpoint. Upper left: Pluto velocity profile overlain by a dipolar coordinate system mesh. Upper right: Unstretched coordinate system from upper left panel underlain by the interpolated velocity profile. Lower right: Four superimposed broadband wavefields (at 1.0s, 2.2s, 3.4s, and 4.6s) propagated through the velocity model in the upper right. Lower left: Wavefields from the lower right interpolated to Cartesian. jeff1-FMexample [ER]

point source propagated outward from the left side of the model. Note that while some energy is lost - for example, at boundaries and steeply dipping energy - the bulk of the wavefield is extrapolated at low angles through the model. The bottom left panel shows the wavefield from the bottom right interpolated back to a Cartesian mesh. The rapid near-horizontal advancement of the wavefield through the salt is evident, as are the top-salt reflections arriving at the free surface.

The remainder of this section describes how I perform forward modeling using RWE operators. I present the rationale for using a dipolar coordinate system, detail an approximate approach for incorporating source radiation patterns and free-surface reflections, and describe a wavefield injection approach to back-propagate wavefield residuals.

Dipole Coordinates

One simplifying factor for an RWE approach is using a coordinate system that is (nearly) orthogonal, such as that developed from a potential field distribution (Shragge, 2006b). Accordingly, the coordinate system used in the following investigations is a (nearly) orthogonal mesh derived from the electrostatics potential field distribution, Φ, of a dipole source formed by two static charges

$$\Phi(\mathbf{x}) = \frac{1}{\sqrt{(x-x_1)^2+\xi^2(z-z_1)^2}} - \frac{1}{\sqrt{(x-x_2)^2+\xi^2(z-z_2)^2}}, \tag{14}$$

where $\mathbf{x_1} = [x_1, z_1]$ and $\mathbf{x_2} = [x_2, z_2]$ are the locations of the two unitary-valued static charges, and ξ is an ellipticity factor inducing a vertical stretch.

A dipolar coordinate system can be derived from equation 14 by computing the equipotential surfaces and associated field lines. Figure 3 illustrates this for a dipole of 4 km spacing and a ξ=1 ellipticity factor. The potential field distribution nearby the singularities becomes nearly radially symmetric and mimics the shape of a wavefield emerging from a point source in a homogeneous medium. For simplicity, I force the initial extrapolation surface to be a circular arc that directly matches the point source wavefield. Although this introduces a slight non-orthogonality into an otherwise orthogonal mesh, this is taken into account by the RWE theory (Shragge, 2006a). In addition, I have situated the source point 50m below the free-surface in order to simulate ghost reflections commonly found in marine data. The forward modeled wavefield, $\Psi(\mathbf{s}, \mathbf{r}; \omega)$, is thus generated by extracting from the wavefield the values at the receiver locations on the center line paralleling the free surface at the source depth.

Radiation Patterns and Free-surface

Two additional factors that warrant comment are the effects of source radiation patterns and the free-surface (see sketch in figure 4). A dipolar coordinate system can partially account for these effects. I generate the initial source wavefield by extracting the direct arrival wavelet from a receiver nearby the source point and spreading it across the 180° arc to form a radially symmetric wavefield. To impart a more realistic radiation pattern, I then introduce an angular

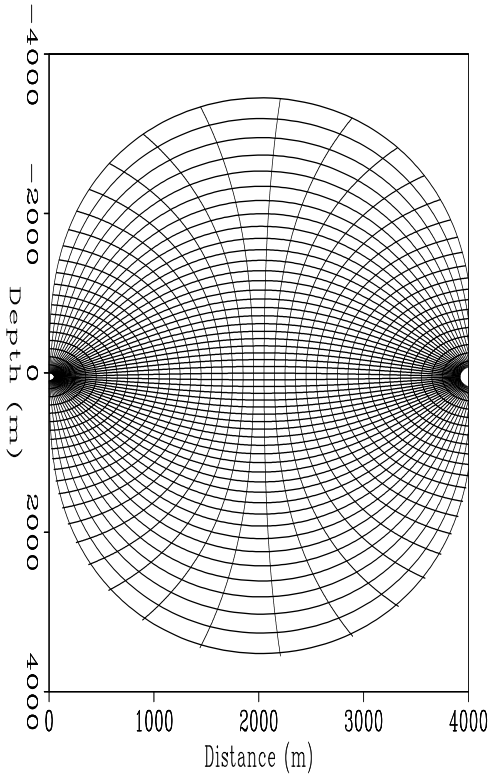

Figure 3: The coordinate system used in the forward modeling tests derived from the potential field and field lines of an electrostatic dipole. jeff1-DipoleRays [ER]

cosine radiation amplitude filter that helps ensure that the wavefield has zero amplitude (at least initially) at the free surface.

Free-surface effects can be approximately incorporated by allowing waves to propagate in a vertically mirrored velocity model. Figure 5 illustrates the expected arrivals from the mirroring procedure. The top panel shows the expected reflected and ghost arrival polarities, while the bottom shows the rays modeled with the mirrored velocity approach. Note that negating the radiation pattern in the mirrored velocity panel generates an effective free-surface ghost, including the R=-1 free-surface reflection coefficient. First-order multiples are also present, but have incorrect polarities that could cause problems in the inversion. Multiples arising from deeper reflectors, though, arrive later and are routinely windowed out from the data.

Forward modeling examples

Figure 6 presents forward modeling results for the Pluto dataset. The left and right panels show the wavefield generated by a fourth-order FD and RWE modeling, respectively. The finite-difference Pluto data on the left is the pressure field component calculated in an elastic model. The RWE data in the right panel are generated according to equation B-14. Note that the reflections apparent near zero-offset in the left panel are completely absent from the right panel. This is because the algorithm cannot propagate reflected waves directly upwards on near-vertical paths because propagation angles are too steep to the extrapolation axis. The

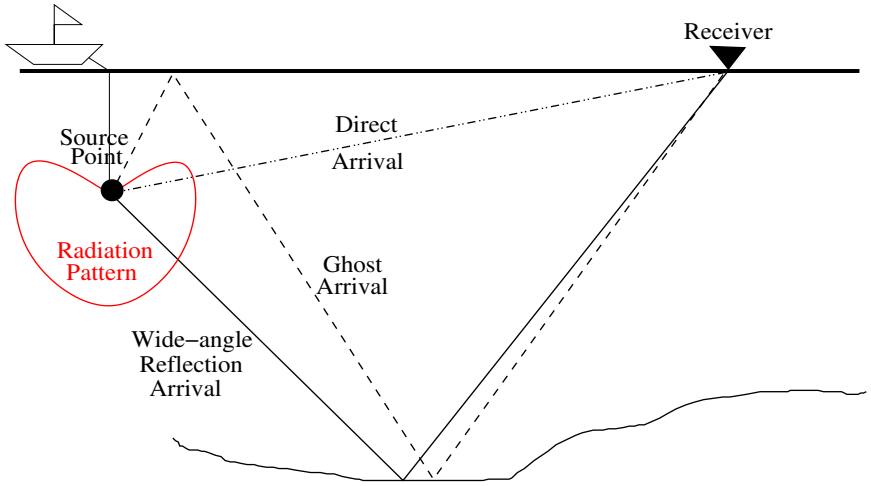

Figure 4: Sketch showing factors complicating modeling wavefield propagation with one-way extrapolation operators. Properly modeling wavefields requires generating multiple arrivals - direct, wide-angle reflections and ghosts - as well as handling the free-surface and source radiation patterns. jeff1-Shot-config [NR]

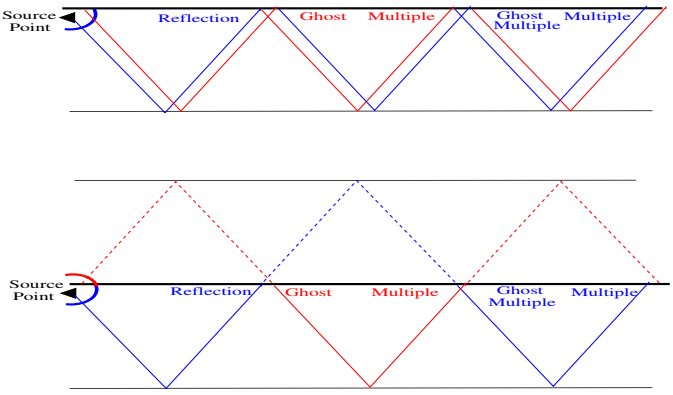

Figure 5: Sketch showing the velocity mirroring process that enables computation of the free-surface reflected ghost. Top panel: Expected ray arrivals. Bottom panel: Calculated arrivals using the mirrored velocity approach. jeff1-mirror [NR]

wavefields at farther offsets (i.e. >16kft), though, become increasingly similar both kinematically and dynamically.

The waveforms input to the inversion algorithm at exploration scale are usually limited to the first few hundred milliseconds after the first arrival. Hence, examining the match between FD and RWE waveforms in this time interval provides insight into the quality of the forward modeling results. Figures 7 and 8 present waveform comparisons at four wide-offsets (>15kft) and four near-offsets (<15kft), respectively. Both waveforms are low-pass filtered to a frequency band typically used for exploration-scale waveform inversion (high corner of 12 Hz). At far offsets the RWE waveforms match those from the FD modeling to a good degree, especially directly after the first arrival. The matches at nearer offsets are fairly poor as expected given the obviously disparate nature of the wavefields shown in figure 6, though show improvements with increasing offset.

Back-projection by wavefield injection

The next step is to develop a procedure for back-projecting the residual wavefield. I use a waveform injection approach based on equation B-15 that is the adjoint operation of extracting data from the wavefield at acquisition depth. An initially zero-valued wavefield is propagated backwards from the farthest receiver toward the source point. As the wavefield reaches each successive receiver location, the residual at that point is injected into the global wavefield and extrapolated to the next step. This process is repeated for all receivers back to the final step closest to the source point. Note that the one-way formulation precludes back-projection of wavefield interactions occurring at a distance farther than the current extrapolation step. (This is the equivalent to an inability to propagate a turning wave upward to the surface in downward continuation.)

Calculating the gradient term in equation 9 is possible after specifying the forward and back-propagation modeling operations. Figure 9 presents an example of a gradient vector for a source and receiver pair separated by 4 km over a mirrored half-space velocity model (upper left panel). The upper right panel shows a monochromatic wavefield propagated forwards from the source point, while the lower right panel shows the wavefield back-propagated from the farthest receiver. The multiplication of these two wavefields is shown in the lower left panel. Woodward (1992), who discusses a similar experiment, terms the result in the lower left "a wavepath" - or the monochromatic analog of a ray-path in the infinite-frequency approximation. Note that the similarity between the wavepath in figure 9 and that of Woodward (1992), whose approach is based on a Rytov approximation.

INVERSION RESULTS

This section details the tests of the waveform inversion procedure described above on a 1D synthetic data model (left panel of figure 10). The velocity perturbation is centered at 1 km depth, is 0.2 km thick, and is 10% greater than the background field of 2 kms^{-1}. The goal of the waveform inversion test is to reconstruct the velocity perturbation starting from an initially

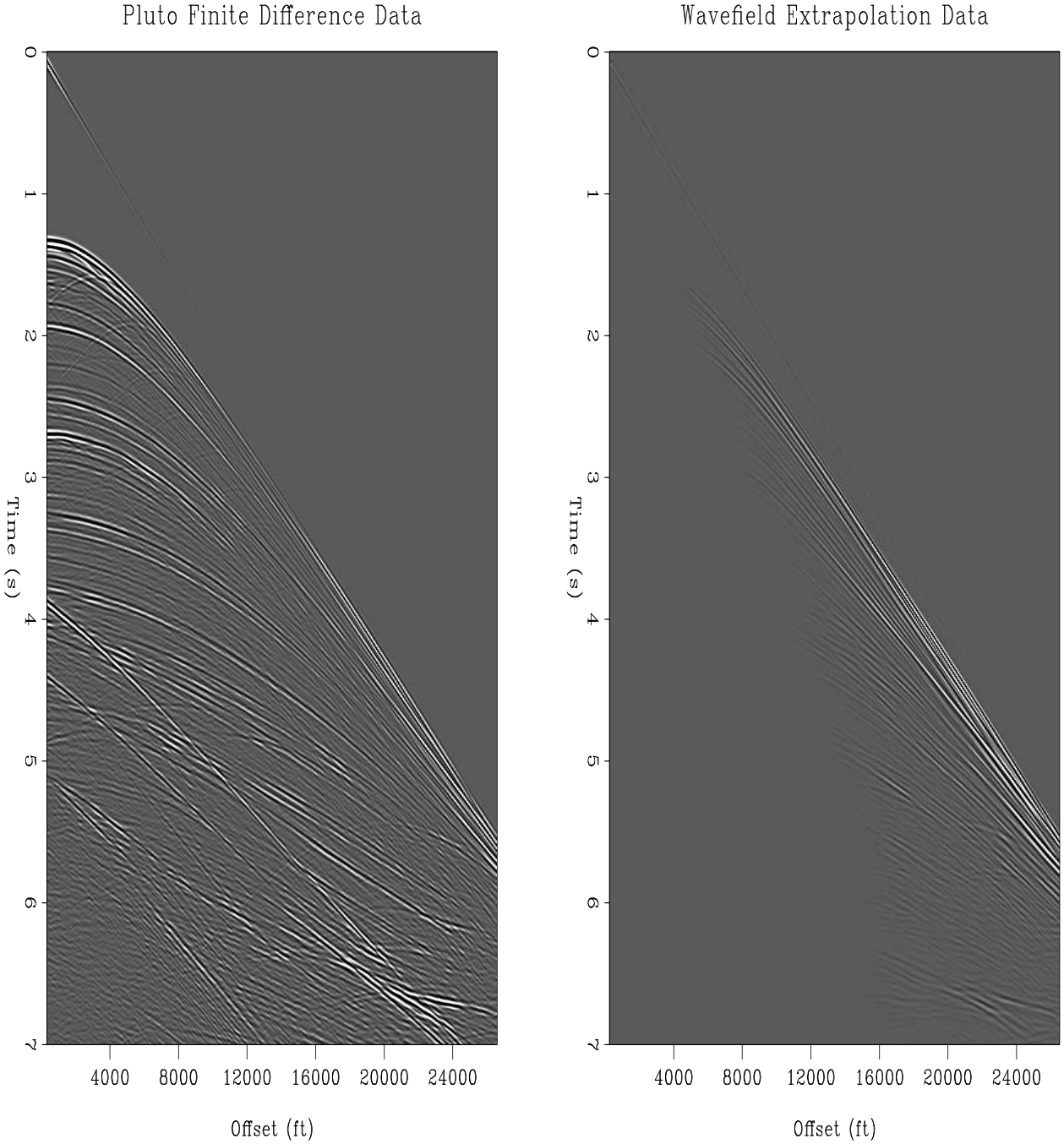

Figure 6: Comparison of the Pluto dataset wavefield generated by a fourth-order finite difference approach (left panel) and the wavefield generated by the RWE modeling approach (right panel) for a source position at 80 kft. jeff1-DataCompare [ER]

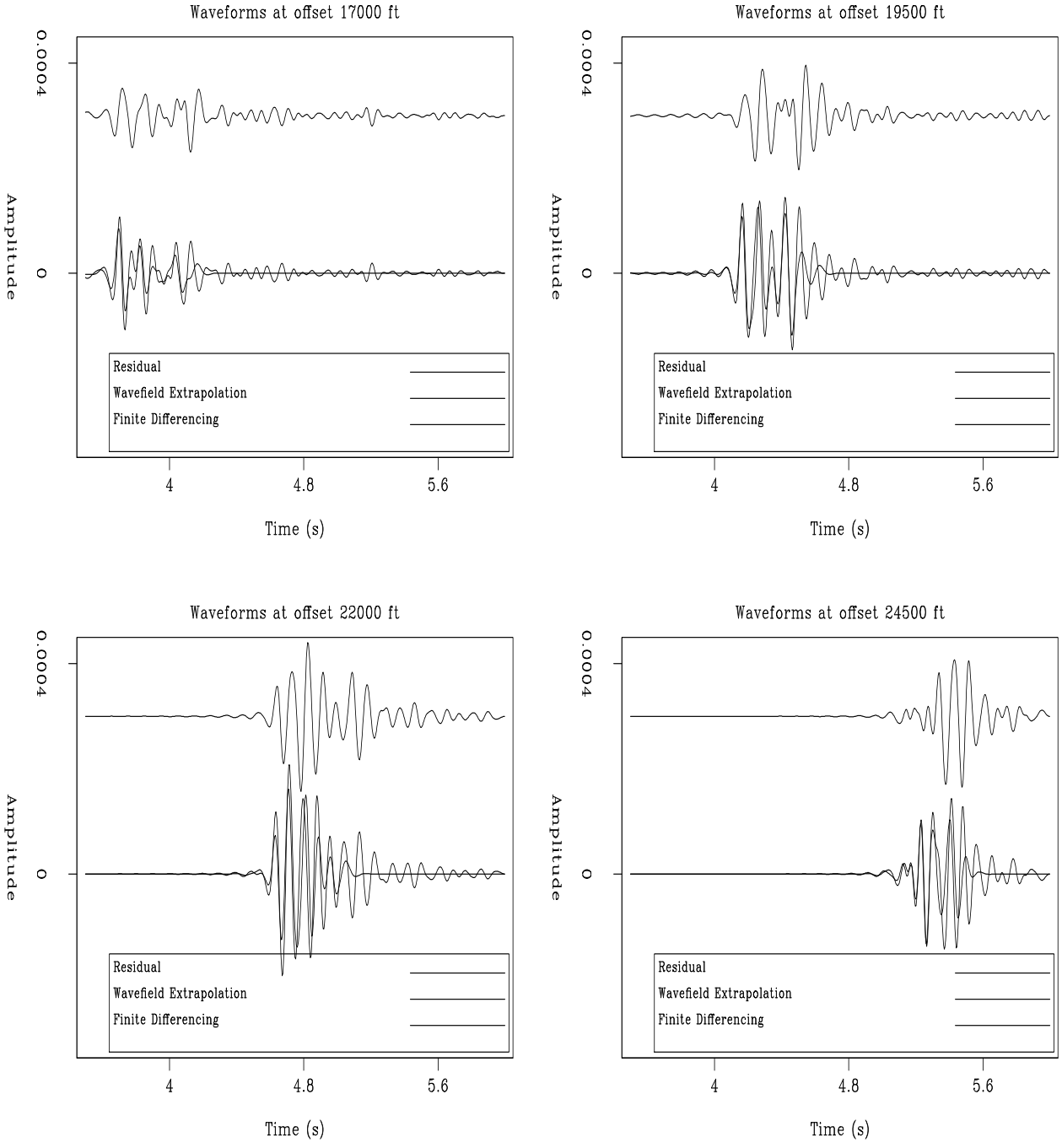

Figure 7: Examples of waveform matching for various wide offsets, with the corresponding residuals for the wavefields shown in figure 6. Top left: 17 kft offset; top right: 19.5 kft offset; bottom left: 22 kft offset; and bottom right: 24.5 kft offset. jeff1-WideOffsets [ER]

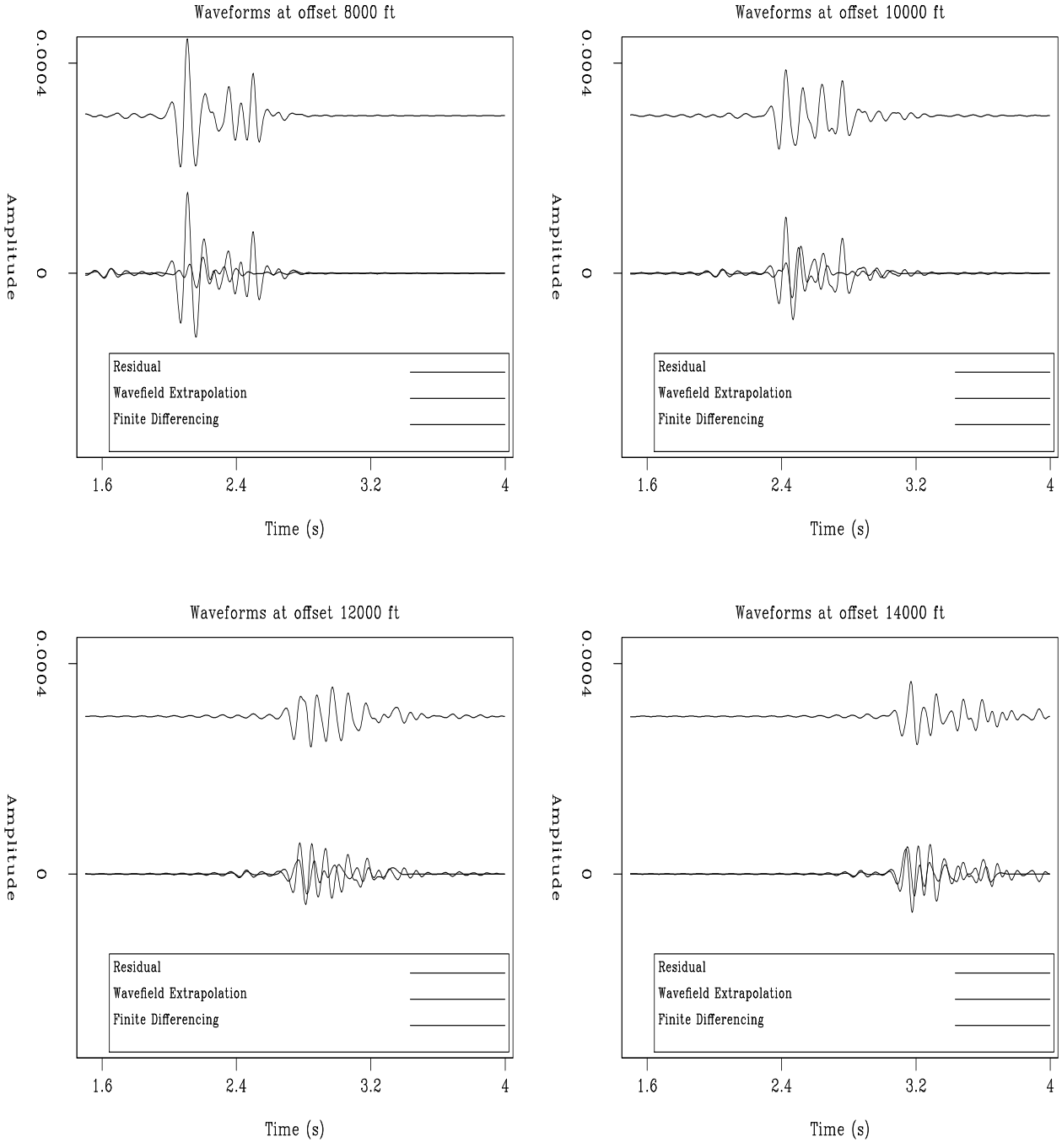

Figure 8: Examples of waveform matching for various near offsets, with the corresponding residuals for the wavefields shown in figure 6. Top left: 8 kft offset; top right: 10 kft offset; bottom left: 12kft offset; and bottom right: 14 kft offset. jeff1-NearOffsets [ER]

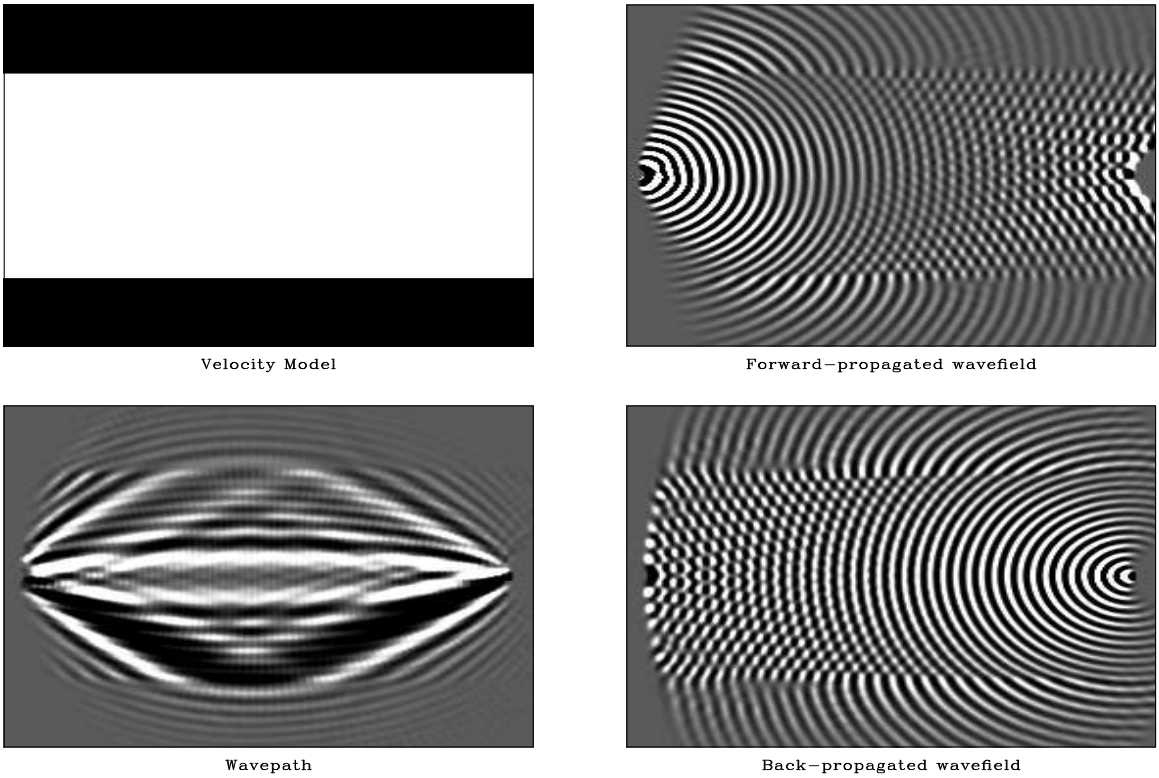

Figure 9: Wavepath example following Woodward (1992). Top left: Half-space velocity model used for synthetic tests. Top right: Forward-propagated wavefield. Bottom right: Back-projected wavefield for a single receiver at 4km offset from source point. Bottom left: Wavepath formed by multiplying wavefields in top and bottom right panels. jeff1-wavepath [ER]

constant velocity model of 2 kms^{-1}. The true velocity profile was input to the SU finite difference modeling package (Stockwell, 1997), which generated data consisting of a linear direct arrival and two reflection hyperbolas of opposing sign (right panel).

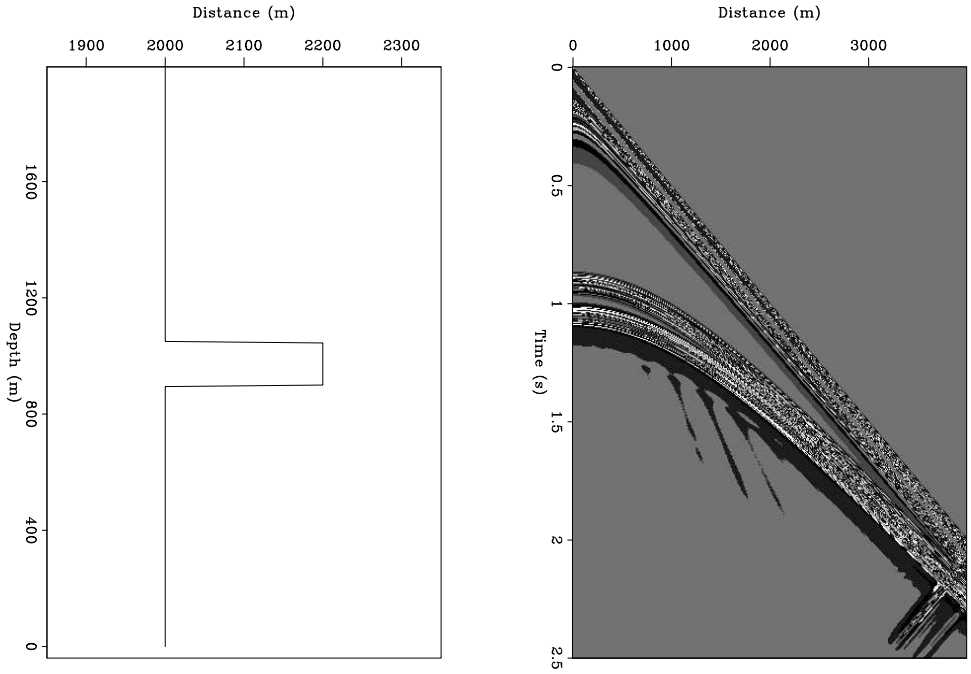

Figure 10: Model used for the waveform inversion test (left panel) and the data generated by FD modeling (right panel). jeff1-ModelData [ER]

Synthetic data were subject to initial preprocessing, including low-pass filtering (high corner of 12Hz), windowing to eliminate boundary artifacts, and zeroing traces < 2 km from the source point. I applied the the latter procedure because the RWE modeling procedure cannot generate accurate wavefield data nearer to the source point. A subset of frequencies ranging from 3-12 Hz in roughly 0.25 Hz intervals were selected for inversion.

Figure 11 presents the waveform inversion results after 5 non-linear iterations. The left panel shows the final estimated perturbation, while the multiple profiles in the right panel show the cumulative velocity perturbation recovered at each integer frequency value between 3-12 Hz. The recovered velocity profile perturbation is centered almost at the correct location. Significant negative side lobes are present both above and below the true perturbation. This observation is somewhat expected because it exhibits a similar phenomenon to that noted in the 1D experimental findings of Sirgue and Pratt (2004).

The recovered perturbation evidently does not contain certain spatial frequency components. One way to better understand this is examining the Fourier spectra of the 1D depth profile (see figure 12). This panel shows the spatial frequency content of both the model and estimated perturbation. The recovered perturbation is lacking energy at the lower frequencies and is somewhat overestimated at mid-range. This observation suggests that the inversion does not use data with either: i) low enough temporal frequencies; or ii) sufficiently wide offsets to

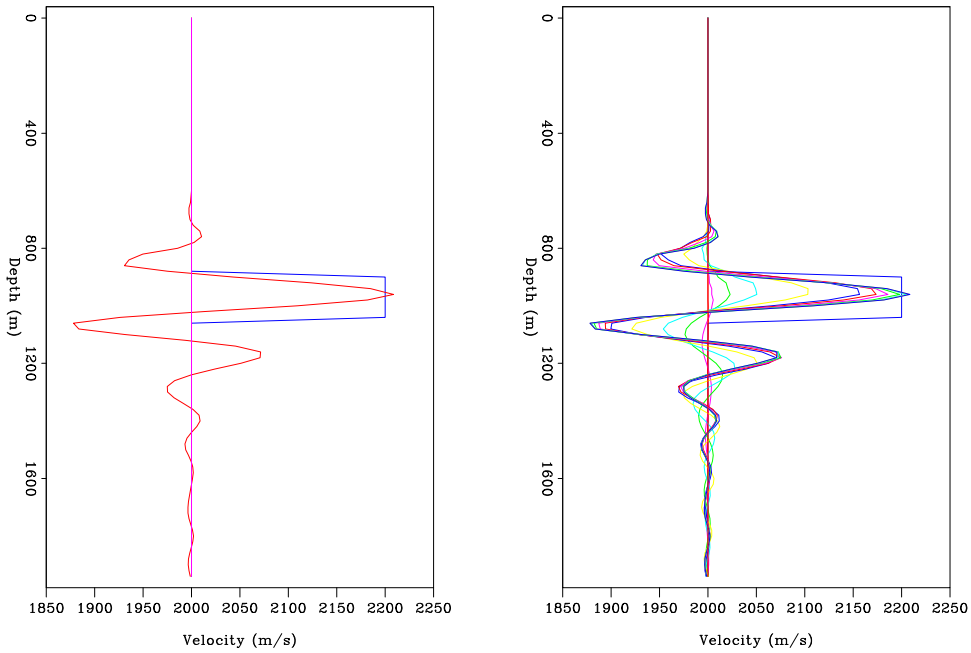

Figure 11: Waveform inversion result for the model and data shown in figure 10 after 5 non-linear iterations in the 3-12 Hz frequency band. Left panel: Recovered vertical velocity profile. Right panel: Vertical velocity profile built up by each successive integer frequency. jeff1-Perturbation [CR]

generate the "image-stretch" phenomena (Sirgue and Pratt, 2004).

One detail important for stabilizing the inversion is to include a near-surface filter on the model space. I implement the filter as a frequency-dependent vertical mask that prevents changes to the velocity model within the first Fresnel zone of the wavepath. The masking operation is essential because it rejects stronger near-surface anomalies that lead to significant non-linear behavior and corresponding wavepath defocusing. I applied no other regularization scheme in the inversion problem solution; however, additional terms could in principle be included.

CONCLUDING REMARKS

This paper presents an alternate forward modeling step of frequency-domain waveform inversion based on operators derived from one-way wave-equations. Wavefield extrapolation is performed on generalized coordinate grids designed to conform to the bulk propagation paths of turning waves. The resulting waveforms are fairly similar to those generated by FD modeling at wider offsets. The results of waveform inversion on synthetic data demonstrate the ability of the approach to invert for moderate velocity perturbations.

The work presented herein shows that the RWE forward modeling approach has significant potential, which motivates additional research on a number of topics. While the next develop-

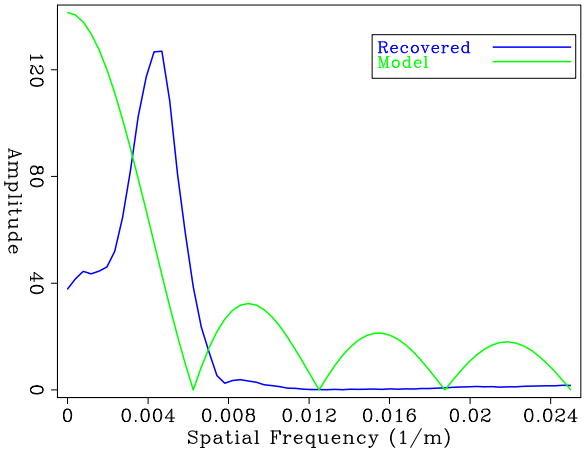

Figure 12: Fourier spectra of the 1D model and recovered perturbation shown in the left panel of figure 11. jeff1-Frequencies [ER]

ment stage would be applying the technique to a 2D dataset, it is important to speculate that this approach should upscale to 3D seismic data volumes with relative ease. This statement is support by the observation that a single iteration of waveform inversion should theoretically be equivalent to a wave-equation migration of three frequencies in a 3D data volume. Importantly, migrations of this size are routine in industry, which suggests that 3D RWE waveform inversion is computationally feasible.

The results also motivate additional work towards improving the amplitude accuracy of the one-way RWE operators. An initial improvement would be including the amplitude factor described by Zhang et al. (2003), which is missing from conventional wavefield extrapolation (Claerbout, 1985). Use of this term should generate data closer to the amplitudes predicted by ray theory. Future work could also implement the one-way operators of Thomson (2005) that derived from a "true-amplitude" one-way wave-equation that incorporates reflection and multiple-scattering losses.

ACKNOWLEDGMENTS

I thank Drew Brenders, Colin Thomson, and Clement Kostov for helpful discussions and acknowledge Schlumberger Cambridge Research for their support during a summer internship where this research was carried out.

REFERENCES

Biondi, B., 2006, 3-D Seismic Imaging: Society of Exploration Geophysicists.

Bunks, C., F. Saleck, S. Zaleski, and G. Chavent, 1985, Multiscale seismic waveform inversion: Geophysics, **60**, 1457–1473.

Claerbout, J., 1985, Imaging the Earth's Interior: Stanford University.

Guggenheimer, H., 1977, Differential Geometry: Dover Publications, Inc., New York.

Lailly, P., 1983, The seismic inverse problem as a sequence of pre-stack migration: Society of Industrial and Applied Mathematics, Bednar, J.B., Redner, R., Robinson, E. and Weglein, A., Eds., Conference on inverse scattering: Theory and Applications.

Liao, Q. and G. McMechan, 1996, Multifrequency viscoacoustic modeling and inversion: Geophysics, **63**, 743–749.

Luenberger, D., 1984, Linear and Nonlinear Programming: 2nd edition: Addison-Wesley.

Mora, P., 1987, Nonlinear two-dimensional elastic inversion of multioffset seismic data: Geophysics, **52**, 1211–1228.

Mulder, W. and R. Plessix, 2006, Full Waveform Tomography and Nonlinear Migration: EAGE, Expanded Abstracts, A038.

Plessix, R., 2006, A Robust Three-Dimensional Iterative Solver for the Time-Harmonic Wave Equation: EAGE, Expanded Abstracts, H047.

Polak, E. and G. Ribiére, 1969, Notes sur la convergence de methodes de directions conjugeés: Revue. Fr. Inf. Rech. Oper., **16-R1**, 35–43.

Pratt, R. and M. Worthington, 1989, The application of diffraction tomography to cross-hole seismic data: Geophysics, **53**, 1284–1294.

Pratt, R., C. Shin, and G. Hicks, 1998, Gauss-Newton and full Newton methods in frequency space seismic waveform inversion: Geophysical Journal International, **133**, 323–340.

Sava, P. and S. Fomel, 2005, Riemannian wavefield extrapolation: Geophysics, **70**, T45–T56.

Shipp, R. and S. Singh, 2002, Two-dimensional full wavefield inversion of wide-aperture marine seismic streamer data: Geophysical Journal International, **151**, 325–344.

Shragge, J., 2006a, Generalized riemannian wavefield extrapolation: SEP–**124**.

Shragge, J., 2006b, Structured mesh generation using differential methods: SEP–**124**.

Sirgue, L. and R. Pratt, 2004, Efficient waveform inversion and imaging: A strategy for selecting temporal frequencies: Geophysics, **69**, 231–248.

Stockwell, J., 1997, Free software in education: A case study of CWP/SU Seismic Un*x: The Leading Edge, **16**, 1045–1049.

Tarantola, A., 1984, Linearized inversion of seismic reflection data in the acoustic approximation: Geophysics, **49**, 998–1015.

Thomson, C., 2005, Accuracy and efficiency considerations for wide-angle wavefield extrapolators and scattering operators: Geophys. J. Int., **163**, 308–323.

Štekl, I. and R. Pratt, 1998, Accurate visco-elastic modeling frequency-domain finite differences using rotated operators: Geophysics, **63**, 1779–1794.

Woodward, M., 1992, Wave-equation tomography: Geophysics, **57**, 15–26.

Zhang, Y., G. Zhang, and N. Bleistein, 2003, True amplitude wave equation migration arising from true amplitude one-way wave equations: Inverse Problems, **19**, 1113–1138.

Zhang, Y., S. Xu, and G. Zhang, 2006, Imaging complex salt bodies with turning-wave one-way wave-equation: Soc. of Expl. Geophys., Expanded Abstracts.

APPENDIX A

Generalized Riemannian Geometry

Geometry in a generalized 3D Riemannian space is described by a symmetric metric tensor, $g_{ij} = g_{ji}$, that relates the geometry in a non-orthogonal coordinate system, $\{x_1, x_2, x_3\}$, to an underlying Cartesian mesh, $\{\xi_1, \xi_2, \xi_3\}$ (Guggenheimer, 1977). In matrix form, the metric tensor is written

$$\left[g_{ij}\right] = \begin{bmatrix} g_{11} & g_{12} & g_{13} \\ g_{21} & g_{22} & g_{23} \\ g_{31} & g_{32} & g_{33} \end{bmatrix} = \begin{bmatrix} g_{11} & g_{12} & g_{13} \\ g_{12} & g_{22} & g_{23} \\ g_{13} & g_{23} & g_{33} \end{bmatrix}, \tag{A-1}$$

where g_{11}, g_{12}, g_{22}, g_{13}, g_{23} and g_{33} are functions linking the two coordinate systems through

$$\begin{aligned} g_{11} &= \frac{\partial x_k}{\partial \xi_1}\frac{\partial x_k}{\partial \xi_1}, \quad g_{12} = \frac{\partial x_k}{\partial \xi_1}\frac{\partial x_k}{\partial \xi_2}, \quad g_{22} = \frac{\partial x_k}{\partial \xi_1}\frac{\partial x_k}{\partial \xi_3}, \\ g_{13} &= \frac{\partial x_k}{\partial \xi_2}\frac{\partial x_k}{\partial \xi_2}, \quad g_{23} = \frac{\partial x_k}{\partial \xi_2}\frac{\partial x_k}{\partial \xi_3}, \quad g_{33} = \frac{\partial x_k}{\partial \xi_3}\frac{\partial x_k}{\partial \xi_3}. \end{aligned} \tag{A-2}$$

(Summation notation - $g_{ii} = g_{11} + g_{22} + g_{33}$ - is used in equations throughout this paper.) The associated (or inverse) metric tensor, g^{ij}, is defined by $g_{ij} = |\mathbf{g}|\, g^{ij}$, where $|\mathbf{g}|$ is metric tensor matrix determinant. The associated metric tensor is given by

$$\left[g^{ij}\right] = \frac{1}{|\mathbf{g}|}\begin{bmatrix} g_{22}g_{33} - g_{23}^2 & g_{13}g_{23} - g_{12}g_{33} & g_{12}g_{23} - g_{13}g_{22} \\ g_{13}g_{23} - g_{12}g_{33} & g_{11}g_{33} - g_{13}^2 & g_{12}g_{13} - g_{11}g_{23} \\ g_{12}g_{23} - g_{13}g_{22} & g_{12}g_{13} - g_{11}g_{23} & g_{11}g_{22} - g_{12}^2 \end{bmatrix}, \tag{A-3}$$

and with the following metric determinant

$$|\mathbf{g}| = g_{33}\left(g_{11}g_{22} - g_{12}^2\right)\left[1 - \frac{g_{11}g_{23}^2 + g_{22}g_{13}^2 - 2g_{12}g_{23}g_{13}}{g_{33}(g_{11}g_{22} - g_{12}^2)}\right]. \tag{A-4}$$

Weighted metric tensor, $m^{ij} = \sqrt{|\mathbf{g}|}\, g^{ij}$, is another useful definition for the following development.

APPENDIX B

One-way Riemannian wavefield extrapolation

The acoustic wave-equation for wavefield, $\mathcal{U}$, in a generalized Riemannian space is

$$\nabla^2 \mathcal{U} = -\omega^2 s^2(\mathbf{x})\, \mathcal{U}, \tag{B-1}$$

where the ω is frequency, s is the propagation slowness, and ∇^2 is the Laplacian operator

$$\Delta \mathcal{U} = \frac{1}{\sqrt{|\mathbf{g}|}}\frac{\partial}{\partial \xi_i}\left(m^{ij}\frac{\partial \mathcal{U}}{\partial \xi_j}\right). \tag{B-2}$$

Substituting equation B-2 into B-1 generates a Helmholtz equation appropriate for propagating waves through a 3D space

$$\frac{1}{\sqrt{|\mathbf{g}|}}\frac{\partial}{\partial \xi_i}\left(m^{ij}\frac{\partial \mathcal{U}}{\partial \xi_j}\right) = -\omega^2 s^2 \mathcal{U}. \tag{B-3}$$

Expanding the derivative terms and multiplying through by $\sqrt{|\mathbf{g}|}$ yields

$$\frac{\partial m^{ij}}{\partial \xi_i}\frac{\partial \mathcal{U}}{\partial \xi_j} + m^{ij}\frac{\partial^2 \mathcal{U}}{\partial \xi_i \partial \xi_j} = -\sqrt{|\mathbf{g}|}\omega^2 s^2 \mathcal{U}. \tag{B-4}$$

Defining n_j as

$$n_j = \frac{\partial m^{ij}}{\partial \xi_i} = \frac{\partial m^{1j}}{\partial \xi_1} + \frac{\partial m^{2j}}{\partial \xi_2} + \frac{\partial m^{3j}}{\partial \xi_3}, \tag{B-5}$$

leads to a more compact notation of equation B-4

$$n_j\frac{\partial \mathcal{U}}{\partial \xi_j} + m^{ij}\frac{\partial^2 \mathcal{U}}{\partial \xi_i \partial \xi_j} = -\sqrt{|\mathbf{g}|}\omega^2 s^2 \mathcal{U}. \tag{B-6}$$

Developing a wave-equation dispersion relation is achieved by replacing the partial differential operators acting on wavefield $\mathcal{U}$ with their Fourier domain duals

$$\left(m^{ij}k_{\xi_i} - i n_j\right)k_{\xi_j} = \sqrt{|\mathbf{g}|}\omega^2 s^2, \tag{B-7}$$

where k_{ξ_i} is the Fourier domain dual of differential operator $\frac{\partial}{\partial \xi_i}$. Equation B-7 represents the dispersion relationship for wavefield propagation on a generalized 3-D Riemannian space.

Solving for the extrapolation wavenumber

Developing an expression for the extrapolation wavenumber requires isolating one of the wavenumbers in equation B-7 (herein assumed to be coordinate ξ_3). Rearranging the results of expanding equation B-7 by introducing indicies $i, j = 1,2,3$ yields

$$\begin{aligned} m^{33}k_{\xi_3}^2 + \left(2m^{13}k_{\xi_1} + 2m^{23}k_{\xi_2} - i\,n_3\right)k_{\xi_3} = \\ \sqrt{|\mathbf{g}|}\omega^2 s^2 + i\left(n_1 k_{\xi_1} + n_2 k_{\xi_2}\right) - m^{11}k_{\xi_1}^2 - m^{22}k_{\xi_2}^2 - 2m^{12}k_{\xi_1}k_{\xi_2}. \end{aligned} \tag{B-8}$$

An expression for wavenumber k_{ξ_3} can be obtained by completing the square

$$\begin{aligned} m^{33}\left(k_{\xi_3} + \tfrac{\left(2m^{13}k_{\xi_1} + 2m^{23}k_{\xi_2} - i\,n_3\right)}{2m^{33}}\right)^2 = \sqrt{|\mathbf{g}|}\omega^2 s^2 - k_{\xi_1}^2\left(m^{11} - \tfrac{\left(m^{13}\right)^2}{m^{33}}\right) - \\ k_{\xi_2}^2\left(m^{22} - \tfrac{\left(m^{23}\right)^2}{m^{33}}\right) - k_{\xi_1}k_{\xi_2}\left(2m^{12} - \tfrac{2m^{13}m^{23}}{m^{33}}\right) + i\,k_{\xi_1}\left(n_1 - \tfrac{m^{13}n_3}{m^{33}}\right) + i\,k_{\xi_2}\left(n_2 - \tfrac{m^{23}n_3}{m^{33}}\right) - \tfrac{n_3^2}{m^{33}}. \end{aligned} \tag{B-9}$$

Isolating wavenumber k_{ξ_3} yields

$$k_{\xi_3} = -a_1 k_{\xi_1} - a_2 k_{\xi_2} + i a_3 \pm \left[a_4^2\omega^2 - a_5^2 k_{\xi_1}^2 - a_6^2 k_{\xi_2}^2 - a_7 k_{\xi_1}k_{\xi_2} + a_8 i\,k_{\xi_1} + a_9 i\,k_{\xi_2} - a_{10}^2\right]^{\frac{1}{2}}, \tag{B-10}$$

where a_i are non-stationary coefficients given by

$$\mathbf{a} = \left[\frac{g^{13}}{g^{33}} \quad \frac{g^{23}}{g^{33}} \quad \frac{n_3}{2m^{33}} \quad \frac{s}{\sqrt{g^{33}}} \quad \sqrt{\frac{g^{11}}{g^{33}} - \left(\frac{g^{13}}{g^{33}}\right)^2} \quad \sqrt{\frac{g^{22}}{g^{33}} - \left(\frac{g^{23}}{g^{33}}\right)^2} \quad \left[\frac{2g^{12}}{g^{33}} - \frac{2g^{13}g^{23}}{(g^{33})^2}\right] \quad \left[\frac{n_1}{m^{33}} - \frac{m^{13}n_3}{(m^{33})^2}\right] \quad \left[\frac{n_2}{m^{33}} - \frac{m^{23}n_3}{(m^{33})^2}\right] \quad \frac{n_3}{m^{33}} \right]^{\mathbf{T}}. \tag{B-11}$$

Note that the coefficients contain a mixture of m^{ij} and g^{ij} terms, and that positive definite terms, a_4, a_5, a_6 and a_{10} in equation B-10are squared, such that the familiar Cartesian split-step Fourier correction is recovered.

For general 2D situations, the coefficients in equation B-11 reduce to

$$\mathbf{a} = \left[\frac{g^{13}}{g^{33}} \quad 0 \quad \frac{n_3}{2m^{33}} \quad \frac{s}{\sqrt{g^{33}}} \quad \sqrt{\frac{g^{11}}{g^{33}} - \left(\frac{g^{13}}{g^{33}}\right)^2} \quad 0 \quad 0 \quad \left[\frac{n_1}{m^{33}} - \frac{m^{13}n_3}{\left(m^{33}\right)^2}\right] \quad 0 \quad \frac{n_3}{m^{33}} \right]^{\mathbf{T}}, \tag{B-12}$$

while a strictly orthogonal 2D mesh leads to the following coefficients

$$\mathbf{a} = \left[0 \quad 0 \quad \frac{n_3}{2m^{33}} \quad \frac{s}{\sqrt{g^{33}}} \quad \sqrt{\frac{g^{11}}{g^{33}}} \quad 0 \quad 0 \quad \frac{n_1}{m^{33}} \quad 0 \quad \frac{n_3}{m^{33}} \right]^{\mathbf{T}}. \tag{B-13}$$

One-way wavefield extrapolation

The expression for k_{ξ_3} forms the basis for a one-way extrapolation operator that can be used to propagate wavefields on generalized coordinate meshes. This requires that a wavefield at step ξ_3 (i.e., $\mathcal{U}(\xi_3, k_{\xi_1}, k_{\xi_2}; \omega)$) be propagated to the next step $\xi_3 + \Delta\xi_3$ (i.e., $\mathcal{U}(\xi_3 + \Delta\xi_3, k_{\xi_1}, k_{\xi_2}, \omega)$) according to

$$\mathcal{U}(\xi_3 + \Delta\xi_3, k_{\xi_1}, k_{\xi_2}, \omega) = \mathcal{U}(\xi_3, k_{\xi_1}, k_{\xi_2}; \omega)\, \mathrm{e}^{-\mathrm{i}k_{\xi_3}\Delta\xi_3}. \tag{B-14}$$

The back-projection of residuals required for waveform inversion can be implemented easily according to the adjoint process of equation B-14,

$$\mathcal{U}(\xi_3 + \Delta\xi_3, k_{\xi_1}, k_{\xi_2}, \omega) = \mathcal{U}(\xi_3, k_{\xi_1}, k_{\xi_2}; \omega)\, \mathrm{e}^{+\mathrm{i}k_{\xi_3}\Delta\xi_3}. \tag{B-15}$$

Note that the coefficients above are spatially variant which requires employing a typical approach (e.g. split-step Fourier, FFD or phase-screens) for developing a mixed $\omega - \mathbf{x}$ domain exponential operators. This study uses the split-step Fourier approach detailed in Shragge (2006a) using the extrapolation wavenumber k_{ξ_3} defined by equation B-13.